Quantifying diffuse and discrete venting at the Tour Eiffel vent site, Lucky Strike hydrothermal field

Eric Mittelstaedt, Javier Escartin, Nuno Gracias, Jean-Arthur Olive, Thibaut Barreyre, Anne Davaille, Mathilde Cannat, Rafael Garcia

Geochemistry Geophysics Geosystems G3

Article
Volume 13, Number 4
19 April 2012
Q04008, doi:10.1029/2011GC003991
ISSN: 1525-2027

Published by AGU and the Geochemical Society

Quantifying diffuse and discrete venting at the Tour Eiffel vent site, Lucky Strike hydrothermal field

Eric Mittelstaedt
Woods Hole Oceanographic Institution, Woods Hole, Massachusetts 02543, USA (emittelstaedt@whoi.edu)

Javier Escartín
IPGP-CNRS, University of Paris 7, F-75005 Paris, France

Nuno Gracias
Computer Vision and Robotics Group, University of Girona, Girona E-17001, Spain

Jean-Arthur Olive
MIT/WHOI Joint Program in Oceanography, Massachusetts Institute of Technology, Woods Hole, Massachusetts 02543, USA

Thibaut Barreyre
IPGP-CNRS, University of Paris 7, F-75005 Paris, France

Anne Davaille
Fluides, Automatiques et Systèmes Thermiques Laboratoire, Univ. Paris 6, F-91405 Orsay CEDEX, France

Mathilde Cannat
IPGP-CNRS, University of Paris 7, F-75005 Paris, France

Rafael Garcia
Computer Vision and Robotics Group, University of Girona, Girona E-17001, Spain

[1] The relative heat carried by diffuse versus discrete venting of hydrothermal fluids at mid-ocean ridges is poorly constrained and likely varies among vent sites. Estimates of the proportion of heat carried by diffuse flow range from 0% to 100% of the total axial heat flux. Here, we present an approach that integrates imagery, video, and temperature measurements to accurately estimate this partitioning at a single vent site, Tour Eiffel in the Lucky Strike hydrothermal field along the Mid-Atlantic Ridge. Fluid temperatures, photographic mosaics of the vent site, and video sequences of fluid flow were acquired during the Bathyluck'09 cruise (Fall, 2009) and the Momarsat'10 cruise (Summer, 2010) to the Lucky Strike hydrothermal field by the ROV *Victor6000* aboard the French research vessel the "Pourquoi Pas"? (IFREMER, France). We use two optical methods to calculate the velocities of imaged hydrothermal fluids: (1) for diffuse venting, Diffuse Flow Velocimetry tracks the displacement of refractive index anomalies through time, and (2) for discrete jets, Particle Image Velocimetry tracks eddies by cross-correlation of pixel intensities between subsequent images. To circumvent video blurring associated with rapid velocities at vent orifices, exit velocities at discrete vents are calculated from the best fit of the observed velocity field to a model of a steady state turbulent plume where we vary the model vent

radius and fluid exit velocity. Our results yield vertical velocities of diffuse effluent between 0.9 cm s^{-1} and 11.1 cm s^{-1} for fluid temperatures between 3°C and 33.5°C above that of ambient seawater, and exit velocities of discrete jets between 22 cm s^{-1} and 119 cm s^{-1} for fluid temperatures between 200°C and 301°C above ambient seawater. Using the calculated fluid velocities, temperature measurements, and photo mosaics of the actively venting areas, we calculate a heat flux due to diffuse venting from thin fractures of 3.15 ± 2.22 MW, discrete venting of 1.07 ± 0.66 MW, and, by incorporating previous estimates of diffuse heat flux density from Tour Eiffel, diffuse flux from the main sulfide mound of ~15.6 MW. We estimate that the total integrated heat flux from the Tour Eiffel site is 19.82 ± 2.88 MW and that the ratio of diffuse to discrete heat flux is ~18. We discuss the implication of these results for the characterization of different vent sites within Lucky Strike and in the context of a compilation of all available measurements of the ratio of diffuse to discrete heat flux.

Components: 10,600 words, 8 figures, 5 tables.

Keywords: Lucky Strike; diffuse venting; hydrothermal vents; video analysis.

Index Terms: 3017 Marine Geology and Geophysics: Hydrothermal systems (0450, 1034, 3616, 4832, 8135, 8424); 3080 Marine Geology and Geophysics: Submergence instruments: ROV, AUV, submersibles; 8130 Tectonophysics: Heat generation and transport.

Received 5 December 2011; **Revised** 9 March 2012; **Accepted** 15 March 2012; **Published** 19 April 2012.

Mittelstaedt, E., J. Escartín, N. Gracias, J.-A. Olive, T. Barreyre, A. Davaille, M. Cannat, and R. Garcia (2012), Quantifying diffuse and discrete venting at the Tour Eiffel vent site, Lucky Strike hydrothermal field, *Geochem. Geophys. Geosyst.*, *13*, Q04008, doi:10.1029/2011GC003991.

1. Introduction

[2] Approximately 75% (~32 TW) of the Earth's surface heat flux (~43 TW) can be attributed to cooling of the oceanic lithosphere of which a third (~11 TW) is estimated to be due to the circulation of hydrothermal fluids through the oceanic crust [*Stein and Stein*, 1994]. Two classes of hydrothermal fluid flow transport this heat flux: (1) discrete, localized jets of high temperature (predominately ≥300°C) fluids with a black or gray color ("black smokers") [e.g., *Spiess et al.*, 1980; *Von Damm*, 1990] and (2) diffuse, lower temperature (predominately ≤100°C), colorless or white fluids which escape through fractures, porous rock, and sediment [*Fisher and Becker*, 1991; *Baker et al.*, 1993; *Trivett and Williams*, 1994]. High-temperature fluids are largely chemically isolated as they ascend and exit the seafloor at discrete vents [*Tivey*, 2007], while diffuse fluids are mixtures between high-temperature fluids and seawater that are believed to form in the shallow sub-seafloor [*Cooper et al.*, 2000; *Stein and Fisher*, 2001; *Fornari et al.*, 2004; *Tivey*, 2007]. The relative flux of these two classes of flow is controlled by the depth, lateral extent, and type of heat sources, and the crustal permeability structure. Crustal heat sources include sub-surface magma chambers [e.g., *Singh et al.*, 1999, 2006], dike intrusions occasionally accompanied by surface lava flows [*Haymon et al.*, 1993; *Baker et al.*, 2004; *Haase et al.*, 2009], serpentinization [*Schroeder et al.*, 2002; *Emmanuel and Berkowitz*, 2006], and possibly hot rock [*Bodvarsson*, 1969; *Lister*, 1974; *Lowell and Germanovich*, 1994; *Fornari et al.*, 1998]. The permeability structure of the crust is poorly understood, but is likely controlled by the porosity of basaltic lavas, the style and rate of eruptions, the location of eruptive conduits, the presence and growth of faults and fractures, and the precipitation of minerals by hydrothermal fluids [*Fisher and Becker*, 1991; *Fornari et al.*, 2004; *Tolstoy et al.*, 2008; *Haase et al.*, 2009; *Hayman and Karson*, 2009; *Crone et al.*, 2010]. The relative heat flux carried by diffuse versus discrete flow may provide an indirect constraint on the crustal permeability structure and thus the circulation of hydrothermal fluids, but few such measurements exist.

[3] Estimates of the heat flux carried by diffuse effluent alone range from 0% to 100% of the total axial heat flux and vary depending upon the vent field and the measurement technique [*Rona and Trivett*, 1992; *Schultz et al.*, 1992; *Baker et al.*, 1993; *Ginster et al.*, 1994; *Elderfield and Schultz*, 1996; *Stein and Fisher*, 2001; *Nielsen et al.*, 2006;

Ramondenc et al., 2006; *Veirs et al.*, 2006; *German et al.*, 2010]. Based upon a compilation of water column surveys of the non-buoyant plume above the Rainbow hydrothermal field, *German et al.* [2010] found that the diffusive component of the flow was below their detection limit and does not significantly contribute to the heat flux there. In contrast, at 9°50′N on the East Pacific Rise (EPR), flow measurements by *Ramondenc et al.* [2006] suggest that the integrated heat flux carried by diffuse flow may be 10 to 1000 times that carried by discrete smoker fluids. At the Lilliput vent field, *Haase et al.* [2009] found no indication of high-temperature, discrete venting over three surveys between 2005 and 2009, indicating that diffuse venting may be responsible for all the hydrothermal cooling at this site. Other estimates generally fall between these extremes. For example, *Baker et al.* [1993] found diffuse flow to carry ∼67% of the heat flux escaping from the North Cleft hydrothermal field on the Juan de Fuca (JdF) ridge. *Nielsen et al.* [2006] used the chemical and isotopic mass balance of Thallium in hydrothermally altered crust to estimate that diffuse hydrothermal flow extracts 5–80% of the heat supplied by crustal magma chambers. It is clear from this large range of estimates that there is no consensus on how hydrothermal heat flux is partitioned between diffuse and discrete flow, and that this partitioning may strongly depend upon local characteristics of the outflow zone.

[4] The aims of the current study are (1) to demonstrate the effectiveness of newly developed optical techniques for measuring hydrothermal fluid velocities [e.g., *Crone et al.*, 2008; *Mittelstaedt et al.*, 2010], (2) to estimate the partitioning between diffuse and discrete heat flux at a single vent site, and (3) to provide a well-constrained measure of the total heat flux at the Tour Eiffel hydrothermal site in the Lucky Strike hydrothermal field by combining our new measurements of diffuse flow from thin fractures and discrete vents with previous measurements of diffuse heat flux density at Tour Eiffel. Our velocity measurement results show maximum, temporally averaged, vertical diffuse flow velocities from thin fractures between 0.9 cm s^{-1} and 11.1 cm s^{-1} and average diffuse heat flux densities between 0.09 MW m^{-2} and 2.67 MW m^{-2}. Calculated exit velocities from discrete vents are between 22 cm s^{-1} and 119 cm s^{-1} and discrete heat fluxes are between 0.03 MW and 0.18 MW. We estimate a ratio of diffuse to discrete heat flux at Tour Eiffel of ∼18 (i.e., 95% of the heat flux is carried by diffuse flow). We discuss the implication of these results in the context of a compilation of previous measurements of the partitioning of heat flux between diffuse and discrete hydrothermal flow.

2. Lucky Strike Hydrothermal Field and the Tour Eiffel Vent Site

[5] The Lucky Strike hydrothermal field is located at the summit of a volcano situated at the center of the Lucky Strike Segment of the Mid-Atlantic Ridge, approximately 400 km southwest of the Azores Islands (Figure 1). The Lucky Strike segment is nearly uniform in width (∼16 km) with depths >3000 m at the segment ends that rise to ∼1550 m at the volcano summit [*Langmuir et al.*, 1993; *Singh et al.*, 2006]. The ridge segment sits on the topographic swell and volcanic plateau associated with the Azores hot spot although observations suggest that the segment is only mildly influenced by the nearby hot spot [*Thibaud et al.*, 1999; *Crawford et al.*, 2008]. The Lucky Strike volcano reaches ∼300 m above the surrounding seafloor, covers ∼50 km^2, and nearly spans the width of the axial valley. The volcano summit hosts 3 highs that rise ∼150 m above a central depression where erupted lavas pooled and formed a lava lake [*Fouquet et al.*, 1995]. Venting at the Lucky Strike hydrothermal field is believed to be driven by fluid flow along inward dipping normal faults within the volcano which penetrate to the depth of the seismically imaged magma chamber roof, ∼2.8–3.8 km beneath the seafloor [*Singh et al.*, 2006; *Combier*, 2007]. The vent field covers an area of ∼0.64 km^2 and consists of ∼30 vent sites distributed around the lava lake with the largest concentration found to the East [*Ondréas et al.*, 2009; *Barreyre et al.*, 2012]. Previous heat flux estimates for the entire Lucky Strike Hydrothermal Field range from 118 MW [*Wilson et al.*, 1996] to 4300 MW [*Jean-Baptiste et al.*, 1998].

[6] The Tour Eiffel vent site is located at 37°17′N, 32°16.5′W, near the southeast limit of the Lucky Strike hydrothermal field (Figure 1). At its center is a ∼15 m tall sulfide tower built by deposition and precipitation associated with several high-temperature "black smoker" vents with fluids exiting at temperatures up to 304°C (this study). Low temperature diffuse fluids (<40°C) vent from this tower as well as from the surrounding sulfide mound and numerous fractures in the nearby basaltic lavas (Figure 2). Active venting around the Tour Eiffel site is associated with deposition of white bacterial mats and anhydrite that rapidly die

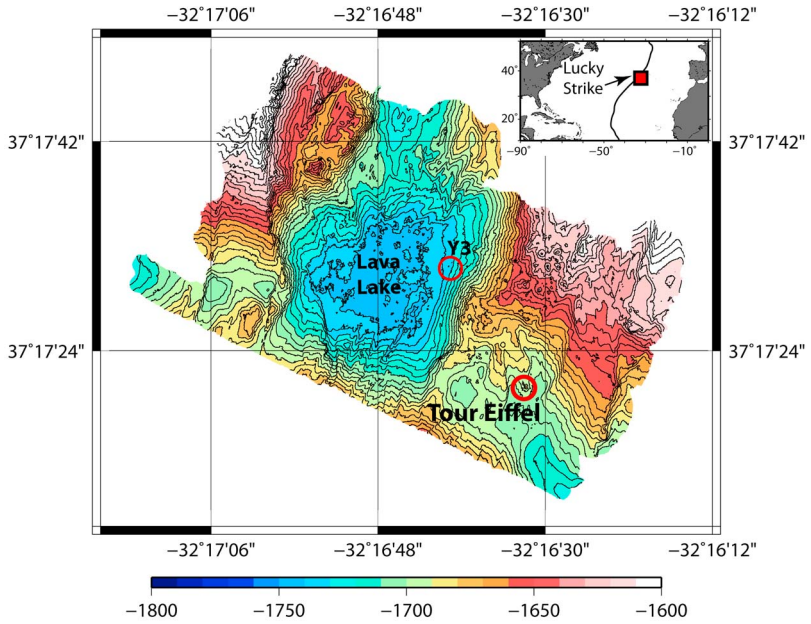

Figure 1. Micro-bathymetry of the Lucky Strike central volcano reveals the location of the sulfide mounds of the vents of the Lucky Strike hydrothermal field. The focus of the current study, the Tour Eiffel vent site (thick, red circle), is located southeast of the lava lake located in the center of the volcano. Diffuse heat fluxes from the Y3 vent site (thin red circle) are discussed in section 6.2. The contour interval is 5 m.

or dissolve, respectively, after the cessation of venting [*Barreyre et al.*, 2012].

3. Data

[7] During the fall of 2009 and summer of 2010, the French research vessel *Pourquoi Pas?* of the Institut Français de Recherche pour l'Exploration de la Mer (IFREMER) carried the Bathyluck'09 and MOMARSAT'10 expeditions to the Lucky Strike Hydrothermal Field. During these expeditions the remote-operated vehicle (ROV) *Victor6000* captured video sequences at the Tour Eiffel vent site of both discrete and diffuse hydrothermal venting along with coincident or nearly coincident temperature measurements using the ROV's temperature probe. The temperatures of discretely venting fluids were measured just before or after video sequences to avoid artificially disturbing the flow, and the temperatures of diffusely venting fluids were collected simultaneously with the video data. The goal of this data collection effort was to apply optical analysis techniques to these video sequences to measure fluid velocities [e.g., *Crone et al.*, 2008, 2010; *Mittelstaedt et al.*, 2010] and to calculate heat fluxes of both types of flow. Diffuse flow imagery was captured principally above fractures around the base of the main sulfide chimney of the Tour Eiffel vent site while discrete flow imagery was captured at smokers at the top of the main tower and at the Aisics vent at the tower base (Figure 2). During Bathyluck'09, we captured several video sequences appropriate for calculation of fluid velocities using optical techniques, including 10 sequences of diffuse flow between 4 s and 40 s in length and 3 sequences of discrete flow between 16 s and 60 s in length. The duration of video sequences was limited primarily by extensive demands on the ROV *Victor6000* to complete other mission objectives. Videos were captured using the main camera of the ROV *Victor6000* with an interlaced resolution of 1440 × 540 pixels (or 1440 × 220 updated pixels per frame) at a rate of 50 frames per second. These video sequences are supplemented by 2 videos each of diffuse and discrete flows from the MOMARSAT'10 expedition. The imaging system of the ROV *Victor6000* was upgraded between these two cruises and the more recent imagery has an interlaced resolution of 1920 × 1080 (1920 × 540 updated pixels per frame) at a rate of 50 frames per second.

[8] Image surveys of the Lucky Strike hydrothermal field were undertaken in 2008 and 2009 using a high-sensitivity, black and white electronic still camera (OTUS) mounted on the *Victor6000* in a vertical, downward-looking orientation. Georeferenced mosaics created from these image

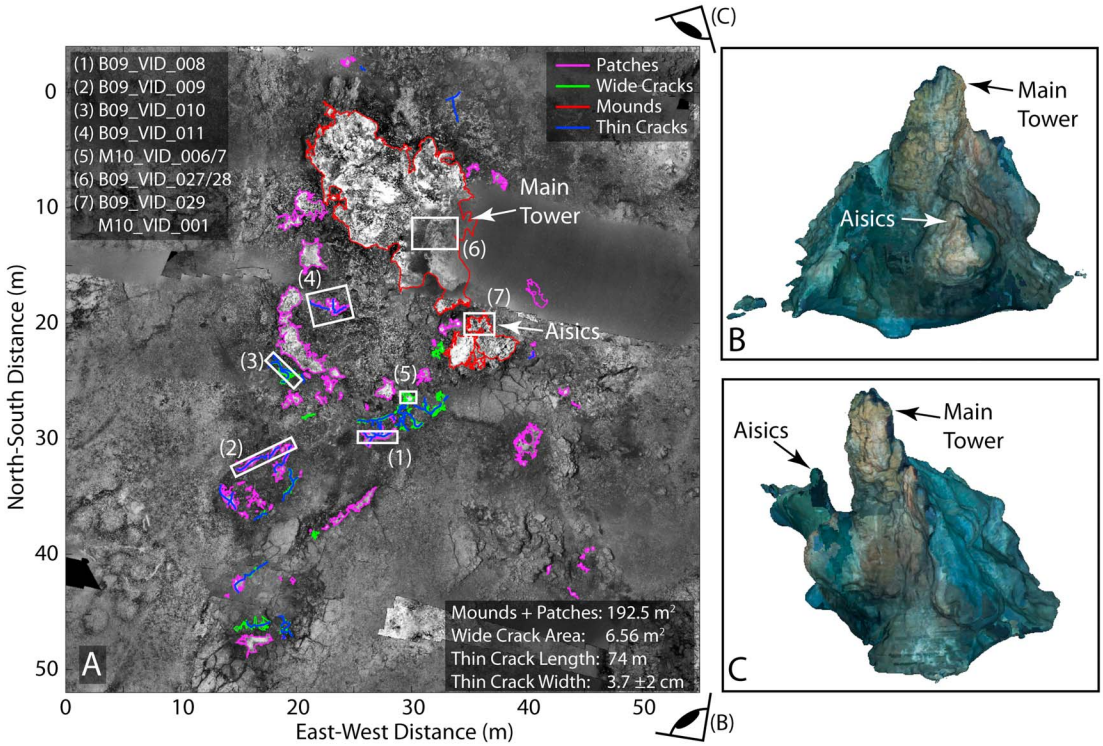

Figure 2. Features of the hydrothermal system at the Tour Eiffel vent site are quantified using (a) a photo-mosaic constructed from images captured at an altitude of ~10 m above the seafloor by the ROV *Victor6000* (IFREMER) [*Barreyre et al.*, 2012]. Around the Tour Eiffel site, diffuse effluent rises from cracks that vary in width from wide (green contours) to thin (blue lines) and from biological mats on the main sulfide mound (red contours), and on the surrounding seafloor (magenta contours). (b, c) Three dimensional reconstructions of the Tour Eiffel edifice provide a perspective view of the main hydrothermal mound [*Garcia et al.*, 2011]. Approximate view orientations are indicated by the abstract eye symbols at the corners of the mosaic. Video sequences used in this study captured diffuse and discrete flows within portions of the white boxes. Sequence names from Bathyluck'09 begin as B09 while those from Momarsat'10 begin as M10.

surveys [*Barreyre et al.*, 2012] allow a detailed characterization of the spatial distribution and style of venting across the Tour Eiffel site (Figure 2a). Such a map is essential to an accurate estimation of the heat flux from a hydrothermal site. Following *Barreyre et al.* [2012], we define 4 types of surfaces with active, diffuse flow: (1) hydrothermal sulfide *mounds*, (2) *patches* associated with white bacterial mats or anhydrite deposition, (3) *thin cracks* which act like linear vents, and (4) *wide cracks* which are equivalent to *patch*-like areas surrounding *thin cracks*. For further details on these definitions and analysis of the photo mosaics, see *Barreyre et al.* [2012].

4. Diffuse Venting From *Thin Cracks*

[9] Diffuse flow at the Tour Eiffel vent site is measured along several *thin cracks* bordering the main venting region (Figure 2). Estimates of the diffuse heat flux from *mounds* and *patches* are discussed in section 6.1. Along these *thin cracks*, pervasive diffuse flow is punctuated by localized, relatively rapid venting from small, individual orifices. Fluids exiting these localized vents have slightly elevated temperatures relative to other diffuse flow (~30–60°C versus ~10–30°C). The spacing of these localized vents is irregular suggesting that they are likely controlled by the local porosity structure of the shallow subsurface. Numerous types of vent fauna are observed along the fractures including mussels, crabs, and shrimp. Additionally, a white biological mat is present at all locations of active diffuse venting.

4.1. Diffuse Fluid Velocities

[10] We use a recently developed method, Diffuse Flow Velocimetry (DFV) [*Mittelstaedt et al.*, 2010], to measure the velocities of diffuse vent fluids as they rise from *thin cracks* on the seafloor. DFV analyzes video sequences of a motionless, random

Table 1. Measured Temperatures Along Tour Eiffel Fractures

Measurement	Corresponding Video Sequence[a]	Temperature (°C)
B09_TEM_008a	B09_VID_008c	38.50
B09_TEM_009d	B09_VID_009c	11.00
B09_TEM_010e	B09_VID_010a (1, 2)	13.50
B09_TEM_011b	B09_VID_011b (1, 2)	16.11
B09_TEM_011c	B09_VID_011c (1, 2)	11.50
B09_TEM_011d	B09_VID_011d	10.00
B10_TEM_001	B10_VID_006/007	13.36
AVERAGE (all)		17.50[b]

[a]For B09_VID_010b, we use the average measured temperature as no measurement was available during this video sequence.
[b]Based upon all measurements above *thin cracks* during Bathyluck'09 and MOMARSAT'10.

medium (e.g., rocks) obtained through the lens of a moving refraction index anomaly (e.g., a hot upwelling) in a two-part calculation. The first step calculates the change in apparent deformation between subsequent background images and the second determines the movement of the apparent deformation through time to determine the fluid velocities. In the first step of the DFV method, the deformation field is determined using Particle Image Velocimetry (PIV), for which we use the LaVision DaVis software (http://www.lavision.de/en/), as discussed in the works of *Davaille and Limare* [2007] and *Limare et al.* [2008]. The second step calculates the displacement of the deformation field from step 1 with MATLAB® scripts that are available as supplementary material in the study by *Mittelstaedt et al.* [2010]. Both steps utilize a cross correlation procedure to determine the highest probability displacement of a portion of an image frame using either pixel intensities (step 1) or deformation vectors (step 2).

[11] Outliers in the velocity calculation can occur due to poor image quality, little or no fluid movement, and/or undetectable deformation (due to very small, very large, or non-existent density variations). Three methods are used to limit false correlations in step 2 of the DFV calculations. First, the velocity is considered valid only if the curvature in the immediate neighborhood of the correlation minimum is greater than an empirically determined critical value of 1×10^{-3} to 1×10^{-4}. Second, a correlation minimum is considered invalid if it falls on the boundary of a correlation matrix. If a correlation minimum does not have a sufficient curvature or falls on the edge of the correlation matrix, it is assumed to be erroneous and the velocity in that location is set to 0. Finally, the calculated velocities are smoothed by a 3x3 median filter. For further details on the DFV method, see *Mittelstaedt et al.* [2010].

4.2. Diffuse Heat Flux

[12] For each video sequence where fluid velocities are calculated using DFV, the diffuse heat flux $q_{diffuse}$ is calculated at each velocity measurement location in the image frame as

$$q_{diffuse} = \rho c_p v_z \left(T_{fluid} - T_{ambient}\right) \quad (1)$$

where v_z is the vertical component of the temporally averaged velocity field, ρ is the density of seawater (1030 kg m^{-3}), c_p is the heat capacity of seawater (4000 J kg^{-1} K^{-1}), $T_{ambient}$ is the temperature of ambient seawater at Tour Eiffel (4°C), and T_{fluid} is the diffuse fluid temperature measured during the corresponding video sequence (Table 1). To estimate a single $q_{diffuse}$ for each image sequence, we calculate the mean and standard deviation of all the heat fluxes in the image frame. We then define the minimum and maximum heat flux as one standard deviation above or below the mean value (Table 2). This is equivalent to using the spatial average and standard deviation of v_z in (1). The integrated heat flux due to *thin cracks* is calculated as the average minimum and maximum $q_{diffuse}$ across all the video sequences multiplied by the width d_{crack} and length l_{crack} of *thin cracks* around the Tour Eiffel site. The values of d_{crack} (3.7 ± 2 cm) and l_{crack} (74 m) are measured digitally on the photo mosaic (section 3, Figure 2).

[13] The temporally averaged vertical velocities of diffuse flow above *thin cracks* reach maximum values between 0.9 cm s^{-1} to 11.1 cm s^{-1} and overall average values of 0.4 cm s^{-1} to 6.2 cm s^{-1} (Table 1 and Figure 3). The magnitude of the velocities displays no clear pattern with distance from the main sulfide orifice or along the length of a given *thin crack*. Temporal variations in the spatially averaged vertical velocity within a given video sequence are generally small (Figure 3) and suggest that using a temporally averaged velocity to estimate the heat flux will not significantly bias the results. Using equation (1) and our measurements of d_{crack} and l_{crack}, we estimate a heat flux due to diffuse flow from *thin cracks* around the Tour Eiffel vent site of 3.15 ± 2.22 MW.

5. Discrete Venting

[14] Discrete venting at the Tour Eiffel vent site is constrained to the main sulfide mound. Using video

Table 2. Diffuse Heat Fluxes

Video Sequence	Elapsed Time (s)	v_z – max (cm s^{-1})	v_z – average (cm s^{-1})	Heat Flux – max (MW m^{-2})	Heat Flux – min (MW m^{-2})
B09_VID_008c	4.24	4.2	1.5	2.67	0.67
B09_VID_009c	10.00	1.4	0.5	0.19	0.09
B09_VID_010a (1)[a]	22.48	4.1	1.1	0.54	0.26
B09_VID_010a (2)[a]	22.48	3.4	1.5	0.85	0.19
B09_VID_010b	25.42	8.9	3.7	2.02	1.64
B09_VID_011b (1)[a]	40.24	6.5	3.9	2.23	1.83
B09_VID_011b (2)[a]	11.00	5.1	2.1	1.18	0.66
B09_VID_011c (1)[a]	14.32	0.9	0.4	0.17	0.13
B09_VID_011c (2)[a]	14.32	1.4	0.4	0.16	0.08
B09_VID_011d	6.66	1.0	0.6	0.16	0.12
M10_VID_006	14.08	11.1	6.2	2.94	1.74
M10_VID_007	42.40	8.3	3.1	1.73	1.07

[a]Numbers after a video sequence signify separate processing of regions of the image frame to avoid obstructions.

imagery, we observe ~8 individual smoker vents where high-temperature fluids (204°C–305°C) escape from the sub-surface. However, as some vents may not be captured by video imagery, here we estimate a range between 7 and 10 vents for our heat flux estimate. Fluid velocities above the vent orifices are calculated by applying optical methods to video sequences of discrete flow from 5 vents.

5.1. Fluid Velocities

[15] At the Tour Eiffel vent site, there are two principal difficulties in using optical methods to measure the fluid velocities from discrete smoker vents: (1) the relatively small optical depth of vent fluids (i.e., relatively clear fluids) at this site and (2) smearing of video imagery near the exit orifice of the vents. Fluids exiting discrete smoker vents at

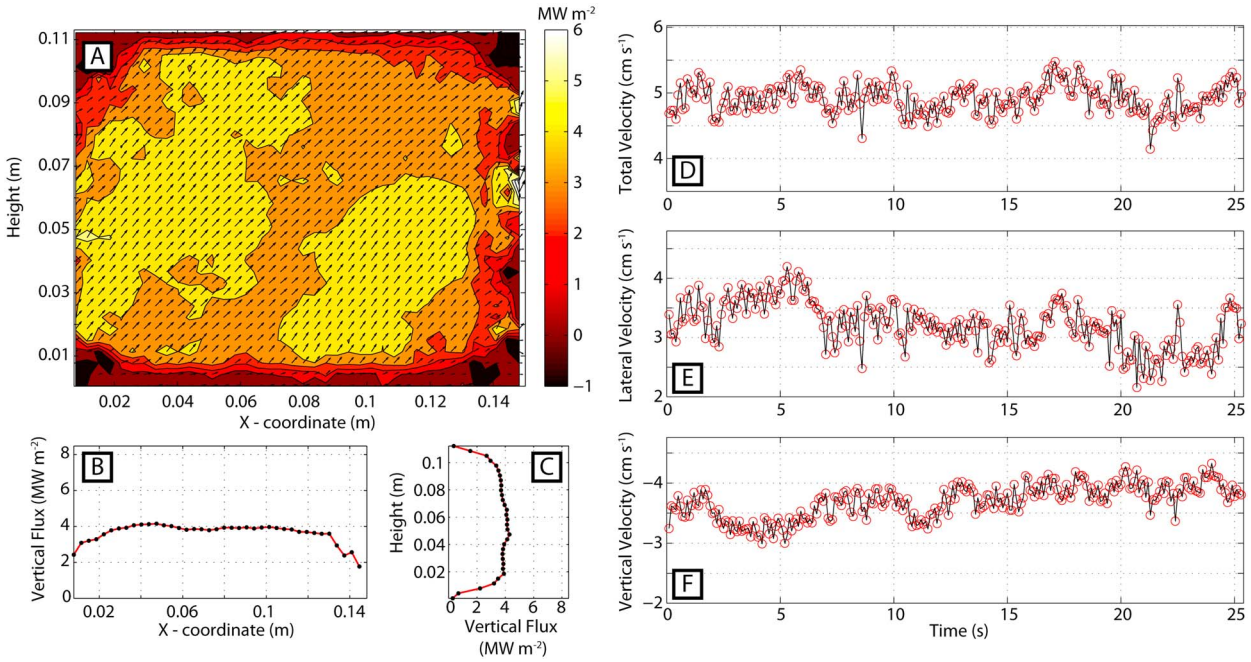

Figure 3. (a) Time-averaged diffuse fluid velocities (black arrows) calculated using DFV from video sequence B09VID010b (see Figure 2 for location). The vertical velocity component is used to calculate the heat flux at each location in the image (colored contours). (b) Vertically and (c) horizontally averaged heat fluxes across the image reveal a spatially uniform heat flux across the majority of the region of interest. Spatially averaged (d) total, (e) lateral, and (f) vertical fluid velocities from each DFV calculation reveal greater variability in the lateral, current-driven velocity than in the vertical, buoyancy-driven fluid flow.

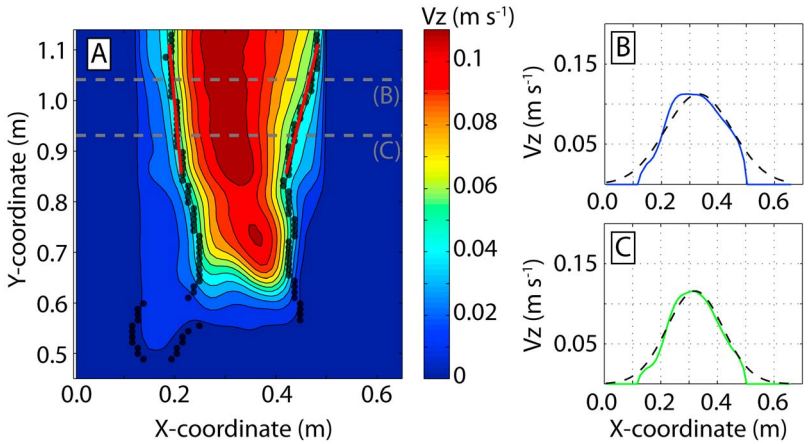

Figure 4. (a) The vertical velocities (filled contours) of hydrothermal fluids exiting from a discrete orifice are measured using PIV. The full width at half maximum (black dots) of horizontal profiles (gray dashed lines) of vertical velocity are used to fit (b, c) Gaussian profiles at each height where velocities are calculated. The width of these Gaussians is used to determine $r_{PIV}(z)$ (section 5.2) within the depth region of interest (red lines).

the Lucky Strike hydrothermal field are lower in temperature (~300°C) than those observed at other high-temperature vents such as at the 9°50′N field on the East Pacific Rise (EPR) where temperatures commonly reach 350°C–375°C [*Von Damm et al.*, 1995; *Fornari et al.*, 1998]. These lower temperature vents have a smaller optical depth, allowing light to more easily traverse the plume because less material precipitates upon interaction with ambient seawater. This causes difficulties for optical methods as the portion of the flow the technique "sees" may vary in time and space. Additionally, any portions of video where background objects are visible behind a flow cannot be used. Smearing of video imagery in the fastest part of the flow (near the exit orifice) where fluid crosses multiple pixels during a single exposure also makes calculation of exit velocities difficult because optical techniques rely on a comparison of pixel intensities between images. To avoid such difficulties, we restrict optical calculations of the fluid velocities to a slower portion of the flow several centimeters above the vent orifice and avoid portions of the video where background objects are visible behind the venting effluent. Exit velocities and orifice radii are subsequently calculated through best fit models to the observed velocity field (section 5.2).

[16] We use a multilevel PIV method identical to the first step in the DFV method (section 4.1) to calculate the fluid velocities from the video imagery. The second cross-correlation step used in DFV is not necessary for smoker fluids because they are generally opaque and tracking of pixel intensities directly yields the fluid velocities, not an apparent background deformation as is the case with diffuse, clear fluids. The resulting fluid velocities are time-averaged through each video sequence (Figure 4). The calculations yield vertical velocities several centimeters above a given orifice on the order of 10 cm s^{-1} (Figures 4 and 5).

5.2. Discrete Heat Fluxes

[17] To estimate the volume and heat flux of black smokers at the Tour Eiffel site, we fit a semi-analytical model of a steady state turbulent jet [*Morton et al.*, 1956; *Speer and Rona*, 1989] to the velocities calculated by PIV. Assuming that steady state flow parameters display similar profiles at all heights and that entrainment of ambient seawater is a depth-dependent function of the characteristic jet buoyancy flux, the equations of conservation of mass, momentum, salinity, and energy describing the velocity v and shape of a steady state turbulent jet are

$$\frac{d}{dz}\left(\rho v r^2\right) = 2\alpha\ vr\bar{\rho} \tag{2}$$

$$\frac{d}{dz}\left(\rho v^2 r^2\right) = r^2 g(\bar{\rho} - \rho) \tag{3}$$

$$\frac{d}{dz}\left(x\rho v r^2\right) = 2\alpha\ vr\bar{x}\bar{\rho} \tag{4}$$

$$\frac{d}{dz}\left(\rho c_p T v r^2\right) = 2\alpha\ vr\bar{\rho}\bar{c}_p\bar{T} \tag{5}$$

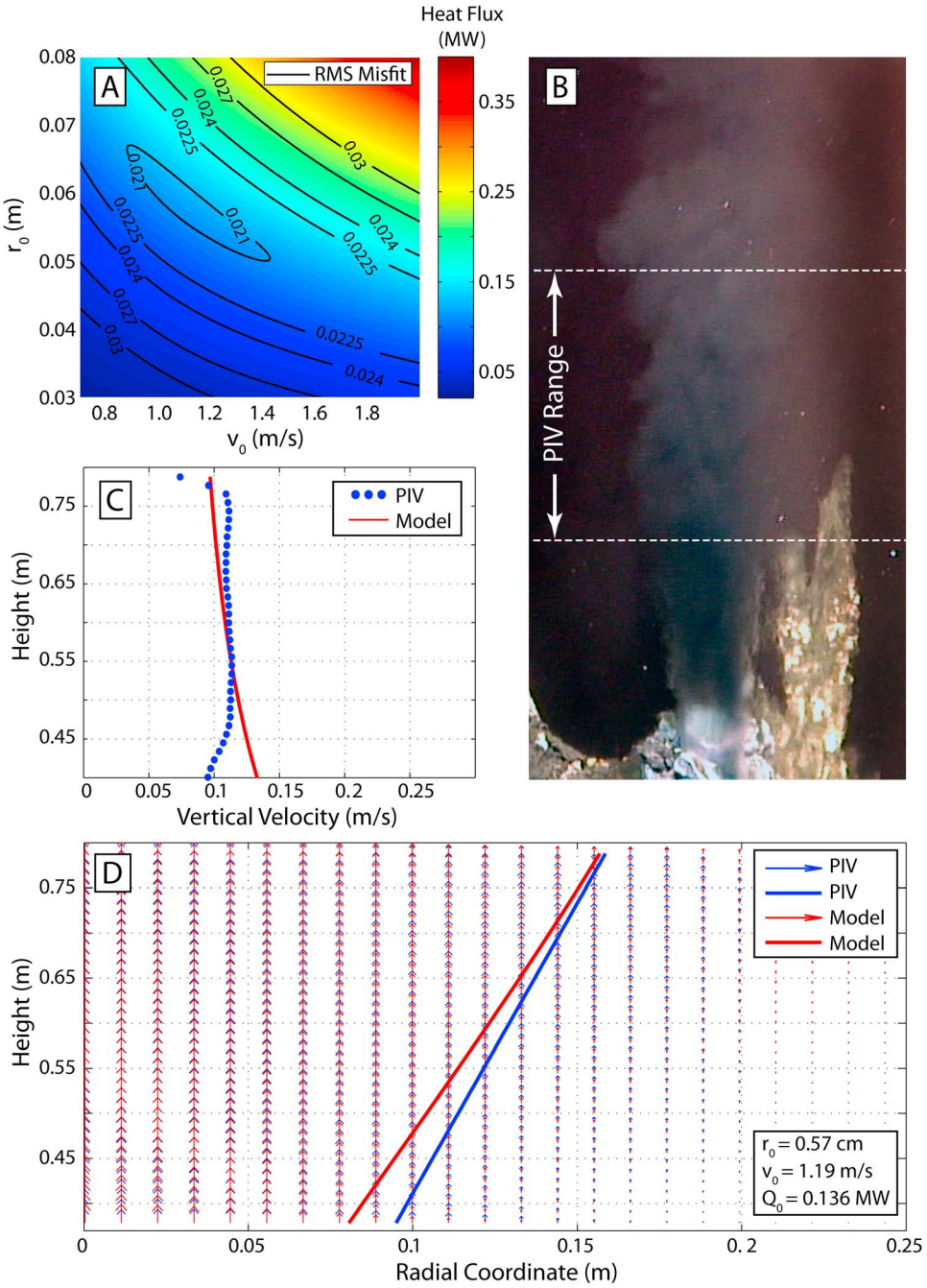

Figure 5. (a) The heat flux (colors) of a smoker vent is determined by a minimum RMS misfit (black contours) model (equations (2)–(5)) where the orifice radius r_0 and exit velocity v_0 are varied. The minimum in RMS misfit tends to contour a constant heat flux, providing a strong constraint on this value. (b) Smoker fluid velocities are calculated on portions of the image where turbulent eddies are clearly distinguished and objects behind the flow are not visible. (c) The best fit model (red line) and PIV centerline velocities match closely in the majority of the flow modeled. (d) The RMS misfit is defined by the difference between models (red) and observations (blue) of vertical velocities (arrows) and the radius of the upwelling plume (lines).

where z is the height above the exit orifice, r is the lateral distance from the jet centerline, α is the depth-dependent entrainment parameter [*Carazzo et al.*, 2008], g is the acceleration of gravity, x is the salinity, T is temperature, and c_p is heat capacity. Barred variables represent the reference values for ambient seawater. In this framework, the flow structure is fully determined by a set of vent source

Table 3. Smoker Heat Fluxes

Video Sequence	Location	Elapsed Time (s)	Heat Flux (MW)	RMS Error	U_0 (cm s^{-1})	R_0 (cm)	T_0 (°C)
B09_VID_027	Main Edifice	16.24	0.14	0.026	70	0.76	300
B09_VID_028	Main Edifice	59.84	0.09	0.019	50	0.87	204
B09_VID_029	Aisics	29.68	0.18	0.030	73	0.83	298
M10_VID_001	Main Edifice	59.58	0.14	0.022	119	0.57	305
M10_VID_011	Aisics	9.00	0.03	0.012	22	0.56	297

conditions (v_0, r_0, x_0, T_0) when the ambient seawater stratification is known. We assume vertical gradients of $\Delta T = 5.4 \times 10^{-4}$ K m^{-1} and $\Delta x = 3.7 \times 10^{-5}$ m^{-1} appropriate for the Atlantic Ocean [*Rudnicki and Elderfield*, 1992]. To complete the set of equations and to determine the appropriate value of c_p, we use an empirical, temperature-dependent equation of state for hydrothermal fluids [*Bischoff and Rosenbauer*, 1985] at constant pressure, and assume that variations in pressure and salinity are identical within seawater and the hydrothermal fluids.

[18] A best fit of the solution to equations (2)–(5) to the observed, time-averaged velocity field is defined as the minimum of the root-mean square (RMS) difference between the model and the PIV calculations of the vertical velocity fields and the depth-dependent flow radii,

$$\Delta_{RMS} = \sqrt{\frac{\sum\left(v_z^{PIV} - v_z^{Analytical}\right)^2}{N}} + \sqrt{\frac{\sum\left(r_{PIV} - r_{Analytical}\right)^2}{n}}, \quad (6)$$

where N is the number of velocity measurements, and n is the number of radius estimates in each image frame. The value of $r_{PIV}(z)$ is defined by the full width at half-maximum (FWHM) of Gaussian curves fit to the vertical velocity profile at each depth in the PIV calculations (Figure 4). To determine the model with the minimum RMS misfit, we hold T_0 and x_0 constant (T_0 is measured at each vent, x_0 is taken to be 30 g kg^{-1}) and systematically vary r_0 and v_0 (Figure 5). Using the best fit model, the discrete heat flux for each vent orifice $q_{discrete}$ is calculated as

$$q_{discrete} = \pi \rho c_p v_0 r_0^2 \left(T_{fluid} - T_{ambient}\right). \quad (7)$$

Finally, we estimate the total discrete heat flux as the mean value of $q_{discrete} \pm$ the standard deviation from all video calculations and subsequently multiplied by the estimated number of discrete vents at Tour Eiffel (7–10). The error bounds on this estimate are defined as the standard deviation of the calculated heat fluxes (Table 3) multiplied by the number of observed vents (7–10).

[19] Exit velocities of our best fit models range between 22 cm s^{-1} and 119 cm s^{-1} from orifices with radii between 0.56 cm and 0.87 cm. The calculated radius of 0.56 cm for B10_VID_011 compares well with that estimated from video data (0.58 cm, Figure 6). Further comparisons between calculated and observed orifice radii were not possible as video data did not provide a clear view of the orifices. The resulting heat fluxes range from 0.03 to 0.18 MW from each discrete vent and yield a mean flux of 0.12 MW with a standard deviation of 0.06 MW (Table 3). We estimate a minimum integrated discrete heat flux as the mean flux minus the standard deviation, multiplied by 7 vents. A maximum estimate is calculated as the mean heat

Figure 6. A cropped image of the vent orifice corresponding to video B10_VID_011. The diameter of the vent orifice (long, red line) is measured based upon the known width of the gas sampler in the image (short, red line). The measured radius (0.58 cm) compares closely with that calculated for B10_VID_011 (0.56 cm).

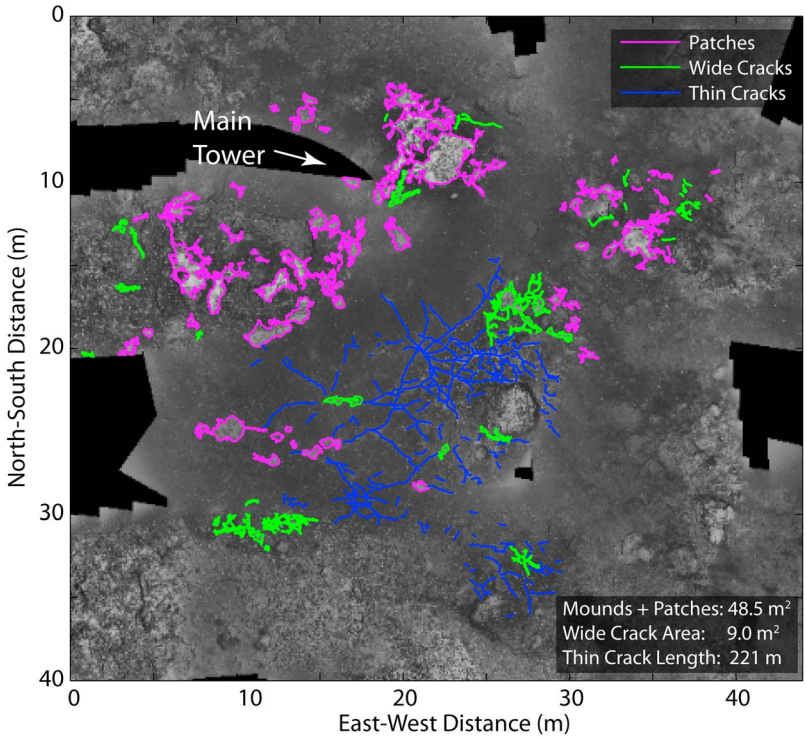

Figure 7. Similarly to Tour Eiffel, features of the hydrothermal system at Y3 are quantified using a photo-mosaic constructed from images captured at an altitude of ~10 m above the seafloor by the ROV *Victor6000* (IFREMER) [*Barreyre et al.*, 2012]. Diffuse effluent rises from cracks that vary in width from wide (green contours) to thin (blue lines) and from biological mats (magenta contours) surrounding the Y3 tower. See text for details.

flux plus the standard deviation, multiplied by 10 vents. These calculations yield an estimated integrated discrete heat flux of 1.07 ± 0.66 MW.

6. Discussion

6.1. Heat Flux at the Tour Eiffel Vent Site

[20] To estimate the total heat flux at Tour Eiffel, we include all diffuse and discrete sources from the sulfide mound and from the surrounding area. We present calculations of the heat carried by low-temperature, diffuse flow from *thin cracks* around the main sulfide mound and high-temperature fluids venting as jets from black smokers. Our collected video data, however, do not permit us to constrain the pervasive diffuse flow exiting from *mounds*, *patches*, and *thick cracks* (i.e., the *patch*-like area around *thin cracks*). To constrain these contributions to the diffuse heat flux, we use a previous measurement of diffuse heat flux density on the Tour Eiffel sulfide edifice of ~0.0781 MW m^{-2} [*Sarrazin et al.*, 2009]. Multiplying this estimate by the area of white substrates (including *patches*, *mounds*, and *thick cracks*) measured in the photo mosaic (199.1 m^2, Figure 2), the total heat flux due to diffuse flow from these areas is ~15.6 MW. Including our calculation of the heat flux from *thin cracks*, we estimate a total diffuse heat flux of 18.75 ± 2.22 MW and, thus, a total heat flux from Tour Eiffel of 19.82 ± 2.88 MW. The resulting ratio of diffuse to discrete heat flux is ~18 with a range between 10 and 51 considering the estimated errors. This suggests that diffuse flow at the Tour Eiffel site carries between 91% and 98% of the total hydrothermal heat flux escaping the seafloor.

6.2. Variability in the Style of Diffuse Venting at Lucky Strike

[21] To investigate how diffuse venting may vary between vent sites within the Lucky Strike vent field, we use our average values of heat flux from *thin cracks*, *patches*, and *wide cracks* at Tour Eiffel to calculate a rough estimate of the diffuse heat flux at the Y3 vent site (Figure 1; 37°17.5′N, 32°16.67′W). As with the Tour Eiffel site, the area of white substrate (57.5 m^2) and the length of *thin cracks* (221 m) are digitized on a high-resolution photo-mosaic (Figure 7) [*Barreyre et al.*, 2012]. These values yield an estimated diffuse flux from

Table 4. Vent Field Estimates of Diffuse and Discrete Heat Flux

Vent Field	Ridge Axis	Diffuse Heat Flux (MW)	Diffuse Fluid Velocity (cm s^{-1})	Discrete Heat Flux (MW)	Discrete Fluid Velocity (cm s^{-1})	Reference
ASHES	Juan de Fuca	45	5–20	4.4	20–90	1
North Cleft	Juan de Fuca	534	-	266	-	2
Middle Valley	Juan de Fuca	270	-	130	-	3
Main Endeavor	Juan de Fuca	9390	7–15	~939[a]	40–50	4
Main Endeavor	Juan de Fuca	5700	-	364	68–337	5
Main Endeavor	Juan de Fuca	292	-	300	-	6
Rainbow	Mid-Atlantic Ridge	No signal	-	500	-	7
9 50′N	East Pacific Rise	950	4	40	10–30	8
Lucky Strike	Mid-Atlantic Ridge	187–1036	-	8–50	-	9

[a]Based upon *Schultz et al.* [1992] estimate of a diffuse to discrete ratio of 10. References: [1], *Rona and Trivett* [1992]; [2], *Baker et al.* [1993]; [3], *Stein and Fisher* [2001]; [4], *Schultz et al.* [1992]; [5], *Ginster et al.* [1994]; [6], *Veirs et al.* [2006]; [7], *German et al.* [2010]; [8], *Ramondenc et al.* [2006]; [9], *Barreyre et al.* [2012].

thin cracks of 9.4 ± 6.6 MW and from white substrate of 4.5 MW. At the Tour Eiffel site, *thin cracks* are responsible for ~16% of the diffuse heat flux, however, at the Y3 site, we estimate that *thin cracks* are responsible for ~67% of the diffuse heat flux. Despite these differences in the style of diffuse flow, the estimates of total diffuse heat flux at Y3 and at Tour Eiffel are statistically similar (13.9 ± 6.6 MW and 18.75 ± 2.2 MW). This suggests that the shallow permeability structure (i.e., differences in total crack length) controls the style of diffuse flow at Y3 and Tour Eiffel. It is unclear, however, if it strongly influences the total diffuse heat flux. The large difference between Y3 and Tour Eiffel in the proportion of the diffuse flow associated with *thin cracks* versus white substrate demonstrates that estimates of heat flux based upon partial or non-existent site characterizations are likely to be poorly constrained. Thus, extrapolation of the Tour Eiffel heat flux to the entire hydrothermal field is unlikely to produce a reliable estimate.

6.3. Comparison to Other Vent Fields and Vent Sites

[22] Of the studies that aim to quantify the total heat flux associated with a hydrothermal vent field on a mid-ocean ridge, only a small subset address how that flux is partitioned between diffuse and discrete venting. The majority of such estimates have been performed on the JdF at the ASHES [*Rona and Trivett*, 1992], North Cleft [*Baker et al.*, 1993], Middle Valley [*Stein and Fisher*, 2001], and Main Endeavor fields [*Schultz et al.*, 1992; *Ginster et al.*, 1994; *Veirs et al.*, 2006] while one estimate was performed on the EPR at the 9°50′N site [*Ramondenc et al.*, 2006], and three exist along the MAR at the Rainbow and Lucky Strike fields [*German et al.*, 2010; *Barreyre et al.*, 2012, this study]. The above studies employ several methods to determine diffuse and discrete heat fluxes including direct flow measurements, water column measurements of temperature and chemistry, borehole and heat flow probes, and mass balance arguments. The ratio of diffuse to discrete heat flux estimated by these studies ranges from 0 at the ultramafic-hosted Rainbow hydrothermal field to almost 25 at the 9°50′N field on the EPR (Table 4 and Figure 8). However, some sites, such as the Lilliput field [*Haase et al.*, 2009] and the off-axis Baby Bare field [*Mottl et al.*, 1998], are devoid of discrete vents altogether which implies that 100% of the hydrothermal heat flux is carried by diffuse flow at these sites.

[23] Figure 8 shows the available values of the diffuse to discrete heat flux ratio (Tables 4 and 5) versus the full spreading rate of the ridge that hosts each hydrothermal field and the depth to the seismically imaged magma lens. There is no discernible trend in the available data. At the intermediate-spreading JdF, values of the heat flux ratio span a large range, even at a single vent field; the estimated ratio of diffuse to discrete heat flux at the Main Endeavor field is between 0.97 and 20 (Tables 4 and 5). The wide distribution of values likely reflects differences in measurement technique, errors due to integration of sparse measurements, and differences in the crustal permeability structure which control hydrothermal circulation, and may suggest that these estimates are biased by the relatively low number of accurate observations that exist. Given the currently available data it is unclear whether this ratio varies systematically between vent fields or individual vent sites, but other observations suggest several magmatic and tectonic processes which may play a role in controlling both

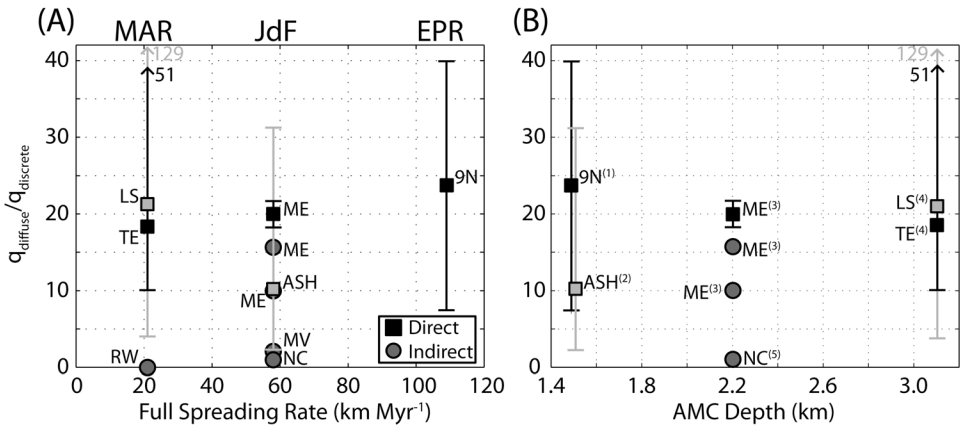

Figure 8. The estimated ratios of diffuse to discrete heat flux $q_{diffuse}/q_{discrete}$ measured using direct (squares) and indirect (circles) methods for vent fields on the Mid-Atlantic Ridge (MAR), Juan de Fuca Ridge (JdF), and East Pacific Rise (EPR) versus (a) spreading rate and (b) depth of the seismically imaged axial magma chamber (AMC). Direct methods involve flow and temperature measurements at vents while indirect methods include water column measurements, seawater chemistry, and sediment heat flow. Estimated errors are shown for direct methods only (lines matching symbol color). Heat flux data are in Tables 4 and 5. The following studies provide estimates of the depth to the AMC: (1) *Harding et al.* [1993], (2) *Carbotte et al.* [2006]; *Baker* [2009], (3) *Van Ark et al.* [2007], (4) *Singh et al.* [2006]; *Crawford et al.* [2008], (5) *Canales et al.* [2006]. Vent fields are identified by the following abbreviations: Tour Eiffel (TE), Lucky Strike (LS), Rainbow (RW), Main Endeavor (ME), ASHES (ASH), Middle Valley (MV), North Cleft (NC), and the 9°N site along the East Pacific Rise (9N).

the local and vent field-scale values of the heat flux ratio.

[24] While it is likely that the ratio of diffuse to discrete venting reflects the permeability structure of the oceanic upper crust, little is known about the processes that quantitatively control these ratios. This is in part due to the complexity of linking the structure of the underlying hydrothermal convection system to its surface manifestations (i.e., venting). Recent modeling work supports a hypothesis that large areas of diffuse venting that connect focused, high-temperature discharge areas may be characteristic of the early stages of formation of a porous upflow zone [*Coumou et al.*, 2009]. In these models, diffuse venting consists of near-surface, low-temperature, positively buoyant fluid, which eventually becomes negatively buoyant, forming a broad recharge zone surrounding a mature, pipe-like discharge area. Such a reduction in diffuse venting with maturation of the convective system is consistent with observations of a decrease in the area of diffuse venting surrounding black smoker vents across the entire Lucky Strike hydrothermal field [*Barreyre et al.*, 2012]. It is inconsistent, however, with the observed dead and dying black smoker systems which point to an overall decrease in hydrothermal output [*Barreyre et al.*, 2012]. *Barreyre et al.* [2012] suggest that the decrease in diffuse and discrete venting across Lucky Strike hydrothermal field is associated with decreasing fluid flow from depth as the axial magma chamber beneath the vent field cools, not development of a mature convective cell.

[25] Another hypothesis is that diffuse venting is controlled by mixing of hot hydrothermal fluids with cold seawater in the shallowest, most permeable extrusive layer [*Wilcock*, 1998]. It is unclear whether this hypothesis should predict a systematic variation in the ratio of diffuse to discrete flux along the global mid-ocean ridge system, and the scarcity and uncertainty of available data cannot settle this question at present. Should a lack of such systematic

Table 5. Vent Site Estimates of Diffuse and Discrete Heat Flux

Vent Site	Vent Field	Ridge Axis	Diffuse Heat Flux (MW)	Discrete Heat Flux (MW)	Reference
Peanut	Main Endeavor	Juan de Fuca	58	2.9[a]	1
Baby Bare	Three Bares	Juan de Fuca, off-axis	2.0–3.0	0	2
Tour Eiffel	Lucky Strike	Mid-Atlantic Ridge	18.75 ± 2.2	1.07 ± 0.66	This study

[a]Discrete flow from smoker at nearby site. References: [1], *Schultz et al.* [1992]; [2], *Mottl et al.* [1998].

variations be established in the future, this will favor a local, shallow (uppermost 100 m below seafloor) control on heat flux partitioning, independent from the regional tectono-magmatic regime. In the following, we focus on the alternative possibility that the ratio of diffuse to discrete venting may systematically vary with changes in large-scale magmatic and tectonic process associated with seafloor-spreading.

[26] Many processes along mid-ocean ridges vary with spreading rate and likely effect hydrothermal circulation either directly or through changes to the thermal or permeability structure of the crust. For example, as spreading rate increases the average depth of magma chambers decreases [*Purdy et al.*, 1992; *Baker*, 2009], eruption frequency increases [*Perfit and Chadwick*, 1998; *Sinton et al.*, 2002], the proportion of sheet flows relative to pillow lavas increases [*Perfit and Chadwick*, 1998], and the spacing of ridge-parallel normal faults and the amount of tectonic strain accommodated by faulting relative to dike injections is predicted to decrease [*Behn and Ito*, 2008; *Goff and Arbic*, 2010]. A global compilation of water column observations shows a strong correlation between the incidence of high-temperature hydrothermal plumes and the depth to magma chambers (data on diffuse fluxes is unavailable) [*Baker*, 2009]. Increasing depth and size of faults with decreasing spreading rate may increase deep circulation of hydrothermal fluids as faults are often invoked as high-permeability conduits which allow fluids to reach the depths of a magma chamber such as observed at the Lucky Strike field [*Singh et al.*, 2006; *Combier*, 2007]. The available data in Figure 8 suggest that these processes do not selectively alter either diffuse or discrete heat flux, but that any changes in hydrothermal circulation lead to uniform modifications in both venting styles. Another possibility, however, is that the large uncertainties of heat flux measurements prevent resolution of any systematic changes with spreading rate.

[27] Observations at the Galapagos Spreading Center (GSC), the Reykjanes Ridge, the Arctic ridges north of Iceland, and the southern MAR support control of the heat flux ratio by magmatic and tectonic processes. Despite the high-magma supply indicated by thick crust on the GSC near the Galapagos hot spot, the incidence of high-temperature hydrothermal plumes is half that expected for the intermediate spreading rate [*Baker et al.*, 2008]. In addition, smoker vents along the GSC are only observed in close proximity to the location of dike-induced fissure systems or caldera collapse features, suggesting that high-permeability fractures are necessary for focused venting [*Haymon et al.*, 2008]. Similarly, on the hot spot-affected Reykjanes Ridge, the incidence of high-temperature plumes is only 20–50% of that observed along other northern MAR segments [*German et al.*, 1994]. To the north of Iceland, along the Arctic ridges, decreases in spreading rate and in inferred magma supply are correlated with an increased incidence of high-temperature plumes in the water column [*Pedersen et al.*, 2008]. Finally, along the southern MAR at the Lilliput field, where the crust is ~11 km thick, no black smoker vents are observed in surveys spanning a period of 4 years [*Haase et al.*, 2009]. The above observations suggest that as crustal thickness (magma supply) increases the incidence of smoker plumes decreases. Although there are likely simultaneous changes in diffuse flux, there are no observations to constrain how diffuse venting varies along these same ridges and whether it indeed has an opposite correlation.

[28] The above observations of decreasing incidence of high-temperature plumes with increasing crustal thickness suggest how tectonic and magmatic processes may control the ratio of diffuse to discrete heat flux. Deformation causing opening of fractures and fissures will allow hydrothermal fluids to rise from deep within the reaction zone, while magmatic eruptions may form shallow barriers to hydrothermal circulation and thus create shallow reservoirs where diffuse fluids form by mixing between hydrothermal fluids and ambient seawater. The volume, style, and frequency of volcanic eruption may be key in determining the resultant ratio of diffuse to discrete heat flux; a high frequency of sheet-type lava flows will cover fractures and cut off access to deep parts of the crust away from a volcanic vent while a large drain-back conduit or caldera collapse will leave pathways to hydrothermal circulation open. For high magma fluxes, a thicker than normal crust may also prevent fluids from reaching the deep, high-temperature heat sources necessary for development of discrete smoker vents. The above processes likely act on the scale of entire vent fields, however, on the smaller scale of individual vent sites such as Tour Eiffel and Y3, and even within a single substrate (e.g., *thin cracks* or *patches*), there is likely to be significant variability in heat flux due to small scale heterogeneities in the crustal permeability structure.

[29] To further constrain the effect of magmatic and tectonic processes on the crustal permeability structure and heat flux partitioning, detailed studies are needed of hydrothermal fields located on ridges

with different spreading rates and magma supplies. Non-invasive techniques such as optical methods [*Crone et al.*, 2008; *Mittelstaedt et al.*, 2010] and recent innovations in acoustic methods [*Rona et al.*, 2010], combined with complete site characterization [*Barreyre et al.*, 2012] promise to significantly improve the accuracy of heat flux measurements at hydrothermal vents.

7. Conclusions

[30] We present results of a video and temperature survey of diffuse and discrete hydrothermal venting at the Tour Eiffel vent site in the Lucky Strike hydrothermal field on the MAR. Using optical techniques, we calculate fluid velocities from 12 video sequences of diffuse flow above *thin cracks* and 5 video sequences of discrete smoker vents. The maximum, temporally averaged, vertical velocities of diffuse effluent range between 0.9 cm s^{-1} and 11.1 cm s^{-1} for fluid temperatures between 3°C and 33.5°C above that of ambient seawater. The calculated exit velocities of discrete jets range between 22 cm s^{-1} and 119 cm s^{-1} for fluid temperatures between 200°C and 301°C above ambient.

[31] We use these velocity calculations and corresponding temperature measurements to estimate the total heat flux from Tour Eiffel and the relative heat carried by diffuse and discrete venting. Diffuse venting from *thin cracks* is estimated to be $\sim 3.15 \pm 2.22$ MW and from discrete vents $\sim 1.07 \pm 0.66$ MW. Incorporating a previous estimate of heat flux density of diffuse flow from bacterial mats on Tour Eiffel's sulfide mound, we estimate that the total diffuse heat flux is 18.75 ± 2.22 MW. These estimates yield a total heat flux from Tour Eiffel of 19.82 ± 2.88 MW with a ratio of diffuse to discrete heat flux of 17.5 (i.e., 95% of the heat flux is carried by diffuse effluent). Significant differences in the style of diffuse venting at the Y3 vent site versus Tour Eiffel demonstrate the need for full characterization of hydrothermal sites to accurately estimate heat flux and suggest that extrapolation of heat flux estimates from a single vent site to an entire vent field is not justified.

[32] Globally, the available measurements of the ratio of diffuse to discrete heat flux span a large range between sites as well as within individual vent fields. The large range of estimates likely reflects the small number of accurate measurements of hydrothermal heat flux. However, this ratio can provide important, indirect evidence for changes in permeability structure and/or spatial distribution and type of heat source at volcanically hosted hydrothermal sites. Observations support the hypothesis that on the scale of an entire hydrothermal field this ratio may be controlled by the rate of fault and fissure formation relative to the rate at which volcanic eruptions pave over these high-permeability conduits.

Acknowledgments

[33] The authors would like to thank the crew of the R/V *Pourquoi Pas?* and the other members of the science party for their aid over the course of this project, as well as the pilots of the ROV *Victor6000* for their aid in collecting the diffuse flow data at the Lucky Strike hydrothermal field. The authors appreciate the detailed reviews of E. Baker and S. White that helped improved the manuscript. E. Mittelstaedt was supported by the International Research Fellowship Program of the U.S. National Science Foundation (OISE-0757920). Funding for the 2006, 2008, 2009, and 2010 cruises was provided by CNRS/IFREMER through the MoMAR program (France), by ANR (France), the Mothseim Project NT05–3 42213 to J. Escartín and by grant CTM2010–15216/MAR from the Spanish Ministry of Science to R. Garcia and J. Escartín. T. Barreyre was supported by University Paris Diderot (Paris 7 – France) and Institut de Physique du Globe de Paris (IPGP, France).

References

Baker, E. T. (2009), Relationships between hydrothermal activity and axial magma chamber distribution, depth, and melt content, *Geochem. Geophys. Geosyst.*, *10*, Q06009, doi:10.1029/2009GC002424.

Baker, E. T., G. Massoth, S. Walker, and R. W. Embley (1993), A method for quantitatively estimating diffuse and discrete hydrothermal discharge, *Earth Planet. Sci. Lett.*, *118*, 235–249, doi:10.1016/0012-821X(93)90170-E.

Baker, E. T., R. P. Lowell, J. Resing, R. Feely, R. W. Embley, G. Massoth, and S. Walker (2004), Decay of hydrothermal output following the 1998 seafloor eruption at Axial Volcano: Observations and models, *J. Geophys. Res.*, *109*, B01205, doi:10.1029/2003JB002618.

Baker, E. T., R. M. Haymon, J. Resing, N. White, S. Walker, G. A. Macdonald, and E. Nakamura (2008), High-resolution surveys along the hot spot-affected Galapagos Spreading Center: 1. Distribution of hydrothermal activity, *Geochem. Geophys. Geosyst.*, *9*, Q09003, doi:10.1029/2008GC002028.

Barreyre, T., J. Escartín, R. Garcia, M. Cannat, and E. Mittelstaedt (2012), Structure, temporal evolution, and heat flux estimates from the Lucky Strike deep-sea hydrothermal field derived from seafloor image mosaics, *Geochem. Geophys. Geosyst.*, *13*, Q04007, doi:10.1029/2011GC003990.

Behn, M., and G. Ito (2008), Magmatic and tectonic extension at mid-ocean ridges: 1. Controls on fault characteristics, *Geochem. Geophys. Geosyst.*, *9*, Q08O10, doi:10.1029/2008GC001965.

Bischoff, J. L., and R. J. Rosenbauer (1985), An empirical equation of state for hydrothermal seawater (3.2 percent NaCl), *Am. J. Sci.*, *285*, 725–763, doi:10.2475/ajs.285.8.725.

Bodvarsson, G. (1969), On the temperature of water flowing through fractures, *J. Geophys. Res.*, *74*, 1987–1992, doi:10.1029/JB074i008p01987.

Canales, J. P., S. C. Singh, R. S. Detrick, S. M. Carbotte, A. J. Harding, G. M. Kent, J. B. Diebold, J. M. Babcock, and M. R. Nedimovic (2006), Seismic evidence for variations in axial magma chamber properties along the southern Juan de Fuca Ridge, *Earth Planet. Sci. Lett.*, *246*, 353–366, doi:10.1016/j.epsl.2006.04.032.

Carazzo, G., E. Kaminski, and S. Tait (2008), On the rise of turbulent plumes: Quantitative effects of variable entrainment for submarine hydrothermal vents, terrestrial and terrestrial explosive volcanism, *J. Geophys. Res.*, *113*, B09201, doi:10.1029/2007JB005458.

Carbotte, S. M., R. S. Detrick, A. J. Harding, J. P. Canales, J. M. Babcock, G. M. Kent, E. Van Ark, M. R. Nedimovic, and J. B. Diebold (2006), Rift topography linked to magmatism at the intermediate spreading Juan de Fuca Ridge, *Geology*, *34*(3), 209–212, doi:10.1130/G21969.1.

Combier, V. (2007), Mid-ocean ridge processes: Insights from 3D reflection seismics at the 9°N OSC on the East Pacific Rise, and the Lucky Strike volcano on the Mid-Atlantic Ridge, PhD thesis, 261 pp., Inst. de Phys. du Globe, Paris.

Cooper, M. J., H. Elderfield, and A. Schultz (2000), Diffuse hydrothermal fluids from Lucky Strike hydrothermal vent field: Evidence for a shallow conductively heated system, *J. Geophys. Res.*, *105*(B8), 19,369–19,375, doi:10.1029/2000JB900138.

Coumou, D., T. Driesner, S. Geiger, A. Paluszny, and C. A. Heinrich (2009), High-resolution three-dimensional simulations of mid-ocean ridge hydrothermal systems, *J. Geophys. Res.*, *114*, B07104, doi:10.1029/2008JB006121.

Crawford, W. C., S. C. Singh, V. Combier, D. Dusunur, and M. Cannat (2008), Crustal structure, magma chamber, and faulting beneath the Lucky Strike Hydrothermal Vent Field, in *Diversity of Hydrothermal Systems on Slow Spreading Ocean Ridges*, *Geophys. Monogr. Ser.*, vol. 188, edited by P. A. Rona et al., pp. 113–132, AGU, Washington, D. C., doi:10.1029/2008GM000726.

Crone, T. J., R. E. McDuff, and W. S. D. Wilcock (2008), Optical plume velocimetry: A new flow measurement technique for use in seafloor hydrothermal systems, *Exp. Fluids*, *45*, 899–915, doi:10.1007/s00348-008-0508-2.

Crone, T. J., W. S. D. Wilcock, and R. E. McDuff (2010), Flow rate perturbations in a black smoker hydrothermal vent in response to a mid-ocean ridge earthquake swarm, *Geochem. Geophys. Geosyst.*, *11*, Q03012, doi:10.1029/2009GC002926.

Davaille, A., and A. Limare (2007), Laboratory studies in mantle convection, in *Treatise on Geophysics*, vol. 7, *Mantle Dynamics*, edited by D. Bercovici, pp. 89–165, Elsevier, Boston, Mass.

Elderfield, H., and A. Schultz (1996), Mid-ocean ridge hydrothermal fluxes and the chemical composition of the ocean, *Annu. Rev. Earth Planet. Sci.*, *24*, 191–224, doi:10.1146/annurev.earth.24.1.191.

Emmanuel, S., and B. Berkowitz (2006), Suppression and stimulation of seafloor hydrothermal convection by exothermic mineral hydration, *Earth Planet. Sci. Lett.*, *243*, 657–668, doi:10.1016/j.epsl.2006.01.028.

Fisher, A. T., and K. Becker (1991), Heat flow, hydrothermal circulation and basalt intrusions in the Guaymas Basin, Gulf of California, *Earth Planet. Sci. Lett.*, *103*, 84–99, doi:10.1016/0012-821X(91)90152-8.

Fornari, D. J., T. M. Shank, K. L. Von Damm, T. K. P. Gregg, M. Lilley, G. Levai, A. Bray, R. M. Haymon, M. R. Perfit, and R. A. Lutz (1998), Time-series temperature measurements at high-temperature hydrothermal vents, East Pacific Rise 9°49′–51′N: Evidence for monitoring a crustal cracking event, *Earth Planet. Sci. Lett.*, *160*, 419–431, doi:10.1016/S0012-821X(98)00101-0.

Fornari, D. J., et al. (2004), Submarine lava flow emplacement at the East Pacific Rise 9°50′N: Implications for uppermost ocean crust stratigraphy and hydrothermal fluid circulation, in *Mid-Ocean Ridges: Hydrothermal Interactions Between the Lithosphere and Oceans*, *Geophys. Monogr. Ser.*, vol. 148, edited by C. R. German, J. Lin, and L. M. Parson, pp. 187–217, AGU, Washington, D. C., doi:10.1029/148GM08.

Fouquet, Y., H. Ondreas, J.-L. Charlou, J.-P. Donval, J. Radford-Knoery, I. Costa, N. Lourenco, and M. K. Tivey (1995), Atlantic lava lakes and hot vents, *Nature*, *377*, 201, doi:10.1038/377201a0.

Garcia, R., R. Campos, and J. Escartín (2011), High-resolution 3D reconstruction of the seafloor for environmental monitoring and modelling, paper presented at International Conference on Intelligent Robots and Systems: Workshop on Robotics for Environmental Monitoring, IEEE, San Francisco, Calif.

German, C., et al. (1994), Hydrothermal activity on the Reykjanes Ridge: The Steinaholl vent-field at 63°06′N, *Earth Planet. Sci. Lett.*, *121*, 647–654, doi:10.1016/0012-821X(94)90098-1.

German, C., A. M. Thurnherr, J. Knoery, J.-L. Charlou, P. Jean-Baptiste, and H. N. Edmonds (2010), Heat, volume and chemical fluxes from submarine venting: A synthesis of results from the Rainbow hydrothermal field 36°N MAR, *Deep Sea Res., Part I*, *57*(4), 518–527, doi:10.1016/j.dsr.2009.12.011.

Ginster, U., M. J. Mottl, and R. P. Von Herzen (1994), Heat flux from black smokers on the Endeavour and Cleft segments, Juan de Fuca Ridge, *J. Geophys. Res.*, *99*(B3), 4937–4950, doi:10.1029/93JB02800.

Goff, J., and B. Arbic (2010), Global prediction of abyssal hill roughness statistics for use in ocean models from digital maps of paleo-spreading rate, paleo-ridge orientation, and sediment thickness, *Ocean Modell.*, *32*, 36–43, doi:10.1016/j.ocemod.2009.10.001.

Haase, K. M., et al. (2009), Diking, young volcansim and diffuse hydrothermal activity on the southern Mid-Atlantic Ridge: The Lilliput field at 9°33′S, *Mar. Geol.*, *266*, 52–64, doi:10.1016/j.margeo.2009.07.012.

Harding, A. J., G. M. Kent, and J. A. Orcutt (1993), A multichannel seismic investigation of upper crustal structure at 9°N on the East Pacific Rise: Implications for crustal accretion, *J. Geophys. Res.*, *98*(B8), 13,925–13,944, doi:10.1029/93JB00886.

Hayman, N. W., and J. A. Karson (2009), Crustal faults exposed in the Pito Deep Rift: Conduits for hydrothermal fluids on the southeast Pacific Rise, *Geochem. Geophys. Geosyst.*, *10*, Q02013, doi:10.1029/2008GC002319.

Haymon, R. M., et al. (1993), Volcanic eruption of the mid-ocean ridge along the East Pacific Rise crest at 9°45–52′N: Direct submersible observations of seafloor phenomena associated with an eruption event in April, 1991, *Earth Planet. Sci. Lett.*, *119*, 85–101, doi:10.1016/0012-821X(93)90008-W.

Haymon, R. M., N. White, E. T. Baker, P. G. Anderson, K. C. Macdonald, and J. Resing (2008), High-resolution surveys along the hot spot-affected Galapagos Spreading

Center: 3. Black smoker discoveries and the implications for geological controls on hydrothermal activity, *Geochem. Geophys. Geosyst.*, *9*, Q12006, doi:10.1029/2008GC002114.

Jean-Baptiste, P., H. Bougault, A. Vangriesheim, J.-L. Charlou, J. Radford-Knoery, Y. Fouquet, H. D. Needham, and C. German (1998), Mantle ^{3}He in hydrothermal vents and plume of the Lucky Strike site (MAR 37°17′N) and associated geothermal heat flux, *Earth Planet. Sci. Lett.*, *157*, 69–77, doi:10.1016/S0012-821X(98)00022-3.

Langmuir, C. H., et al. (1993), Geological setting and characteristics of the Lucky Strike vent field at 37°17′N on the Mid-Atlantic Ridge, *Eos Trans. AGU*, *74*(43), Fall Meet. Suppl., F99.

Limare, A., I. Kumagai, J. Vatteville, and A. Davaille (2008), Thermal plumes visualisation: Differential interferometry versus thermochromic liquid crystals, paper presented at 13th International Symposium on Flow Visualisation, Univ. of Franche-Comté, Nice, France, 1–4 July. [Available at http://www.ipgp.fr/limare/318.pdf.]

Lister, C. R. B. (1974), On the penetration of water into hot rock, *Geophys. J. R. Astron. Soc.*, *39*, 465–509, doi:10.1111/j.1365-246X.1974.tb05468.x.

Lowell, R. P., and L. N. Germanovich (1994), On the temporal evolution of high-temperature hydrothermal systems at ocean ridge crests, *J. Geophys. Res.*, *99*(B1), 565–575, doi:10.1029/93JB02568.

Mittelstaedt, E., A. Davaille, P. E. van Keken, N. Gracias, and J. Escartin (2010), A noninvasive method for measuring the velocity of diffuse hydrothermal flow by tracking moving refractive index anomalies, *Geochem. Geophys. Geosyst.*, *11*, Q10005, doi:10.1029/2010GC003227.

Morton, B. R., G. Taylor, and J. S. Turner (1956), Turbulent gravitational convection from maintained and instantaneous sources, *Proc. R. Soc. London, Ser. A*, *234*, 1–23, doi:10.1098/rspa.1956.0011.

Mottl, M. J., et al. (1998), Warm springs discovered on 3.5 Ma oceanic crust, eastern flank of the Juan de Fuca Ridge, *Geology*, *26*, 51–54, doi:10.1130/0091-7613(1998)026<0051:WSDOMO>2.3.CO;2.

Nielsen, S. G., M. Rehkamper, D. A. H. Teagle, D. A. Butterfield, J. C. Alt, and A. N. Halliday (2006), Hydrothermal fluid fluxes calculated from the isotopic mass balance of thallium in the ocean crust, *Earth Planet. Sci. Lett.*, *251*, 120–133, doi:10.1016/j.epsl.2006.09.002.

Ondréas, H., M. Cannat, Y. Fouquet, A. Normand, P. M. Sarradin, and J. Sarrazin (2009), Recent volcanic events and the distribution of hydrothermal venting at the Lucky Strike hydrothermal field, Mid-Atlantic Ridge, *Geochem. Geophys. Geosyst.*, *10*, Q02006, doi:10.1029/2008GC002171.

Pedersen, R. B., I. H. Thorseth, T. E. Nygard, M. Lilley, and D. S. Kelley (2008), Hydrothermal activity at the Arctic mid-ocean ridges, in *Diversity of Hydrothermal Systems on Slow Spreading Ocean Ridges*, *Geophys. Monogr. Ser.*, vol. 188, edited by P. A. Rona et al., pp. 67–89, AGU, Washington, D. C., doi:10.1029/2008GM000783.

Perfit, M. R., and W. W. Chadwick Jr. (1998), Magmatism at mid-ocean ridges: Constraints from volcanological and geochemical investigations, in *Faulting and Magmatism at Mid-Ocean Ridges*, *Geophys. Monogr. Ser.*, vol. 106, edited by W. Roger Buck et al., pp. 59–115, AGU, Washington, D. C., doi:10.1029/GM106p0059.

Purdy, G. M., L. S. L. Kong, G. L. Christeson, and S. C. Solomon (1992), Relationship between spreading rate and the seismic structure of mid-ocean ridges, *Nature*, *355*, 815–817, doi:10.1038/355815a0.

Ramondenc, P., L. N. Germanovich, K. L. Von Damm, and R. P. Lowell (2006), The first measurements of hydrothermal heat output at 9°50′N, East Pacific Rise, *Earth Planet. Sci. Lett.*, *245*, 487–497, doi:10.1016/j.epsl.2006.03.023.

Rona, P. A., and D. A. Trivett (1992), Discrete and diffuse heat transfer at ASHES vent field, Axial Volcano, Juan de Fuca Ridge, *Earth Planet. Sci. Lett.*, *109*, 57–71, doi:10.1016/0012-821X(92)90074-6.

Rona, P. A., K. G. Bemis, C. Jones, D. R. Jackson, K. Mitsuzawa, and D. R. Palmer (2010), Partitioning between plume and diffuse flow at the Grotto vent cluster, Main Endeavour Field, Juan de Fuca Ridge; Past and Present, Abstract OS21C-1519 presented at 2010 Fall Meeting, AGU, San Francisco, Calif., 13–17 Dec.

Rudnicki, M. D., and H. Elderfield (1992), Theory applied to the Mid-Atlantic Ridge hydrothermal plumes: The finite-difference approach, *J. Volcanol. Geotherm. Res.*, *50*, 161–172, doi:10.1016/0377-0273(92)90043-D.

Sarrazin, J., P. Rodier, M. A. Tivey, H. Singh, A. Schultz, and P. M. Sarradin (2009), A dual sensor device to estimate fluid flow velocity at diffuse hydrothermal vents, *Deep Sea Res., Part I*, *56*(11), 2065–2074, doi:10.1016/j.dsr.2009.06.008.

Schroeder, T., B. E. John, and B. R. Frost (2002), Geologic implications of seawater circulation through peridotite exposed at slow-spreading mid-ocean ridges, *Geology*, *30*, 367–370, doi:10.1130/0091-7613(2002)030<0367:GIOSCT>2.0.CO;2.

Schultz, A., J. R. Delaney, and R. E. McDuff (1992), On the partitioning of heat flux between diffuse and point source seafloor venting, *J. Geophys. Res.*, *97*(B9), 12,299–12,314, doi:10.1029/92JB00889.

Singh, S. C., J. S. Collier, A. J. Harding, G. M. Kent, and J. A. Orcutt (1999), Seismic evidence for a hydrothermal layer above the solid roof of the axial magma chamber at the southern East Pacific Rise, *Geology*, *27*, 219–222, doi:10.1130/0091-7613(1999)027<0219:SEFAHL>2.3.CO;2.

Singh, S. C., W. C. Crawford, H. Carton, T. Seher, V. Combier, M. Cannat, J. P. Canales, D. Dusunur, J. Escartín, and J. M. Miranda (2006), Discovery of a magma chamber and faults beneath a Mid-Atlantic Ridge hydrothermal field, *Nature*, *442*, 1029–1032, doi:10.1038/nature05105.

Sinton, J. M., E. Bergmanis, K. Rubin, R. Batiza, T. K. P. Gregg, K. Gronvold, G. A. Macdonald, and S. M. White (2002), Volcanic eruptions on mid-ocean ridges: New evidence from the superfast East Pacific Rise, 17°–19°, *J. Geophys. Res.*, *107*(B6), 2115, doi:10.1029/2000JB000090.

Speer, K. G., and P. A. Rona (1989), A model of an Atlantic and Pacific hydrothermal plume, *J. Geophys. Res.*, *94*(C5), 6213–6220, doi:10.1029/JC094iC05p06213.

Spiess, F. N., et al. (1980), East Pacific Rise: Hot springs and geophysical experiments, *Science*, *207*, 1421–1433, doi:10.1126/science.207.4438.1421.

Stein, C. A., and S. Stein (1994), Constraints on hydrothermal heat flux through the oceanic lithosphere from global heat flow, *J. Geophys. Res.*, *99*(B2), 3081–3095, doi:10.1029/93JB02222.

Stein, J. S., and A. T. Fisher (2001), Multiple scales of hydrothermal circulation in Middle Valley, northern Juan de Fuca Ridge: Physical constraints on geological models, *J. Geophys. Res.*, *106*(B5), 8563–8580, doi:10.1029/2000JB900395.

Thibaud, R., O. Dauteuil, and P. Gente (1999), Faulting pattern along slow-spreading ridge segments: A consequence of along-axis variation in lithospheric rheology, *Tectonophysics*, *312*, 157–174, doi:10.1016/S0040-1951(99)00165-1.

Tivey, M. A. (2007), Generation of seafloor hydrothermal vent fluids and associated mineral deposits, *Oceanography*, *20*(1), 50–65, doi:10.5670/oceanog.2007.80.

Tolstoy, M., F. Waldhauser, D. Bohnenstiehl, R. T. Weekly, and W. Y. Kim (2008), Seismic identification of along-axis hydrothermal flow on the East Pacific Rise, *Nature*, *451*, 181–184, doi:10.1038/nature06424.

Trivett, D. A., and A. J. I. Williams (1994), Effluent from diffuse hydrothermal venting: 2. Measurement of plumes from diffuse hydrothermal vents at the southern Juan de Fuca Ridge, *J. Geophys. Res.*, *99*(C9), 18,417–18,432, doi:10.1029/94JC00096.

Van Ark, E., R. S. Detrick, J. P. Canales, S. M. Carbotte, A. J. Harding, G. M. Kent, M. R. Nedimovic, W. S. D. Wilcock, J. B. Diebold, and J. M. Babcock (2007), Seismic structure of the Endeavour Segment, Juan de Fuca Ridge: Correlations with seismicity and hydrothermal activity, *J. Geophys. Res.*, *112*, B02401, doi:10.1029/2005JB004210.

Veirs, S. R., R. E. McDuff, and F. R. Stahr (2006), Magnitude and variance of near-bottom horizontal heat flux at the Main Endeavour hydrothermal vent field, *Geochem. Geophys. Geosyst.*, *7*, Q02004, doi:10.1029/2005GC000952.

Von Damm, K. L. (1990), Seafloor hydrothermal activity: Black smoker chemistry and chimneys, *Annu. Rev. Earth Planet. Sci.*, *18*, 173–204, doi:10.1146/annurev.ea.18.050190.001133.

Von Damm, K. L., S. E. Oosting, R. Kozlowski, L. G. Buttermore, D. C. Colodner, H. N. Edmonds, J. M. Edmond, and J. M. Grebmeier (1995), Evolution of East Pacific Rise hydrothermal vent fluids following a volcanic eruption, *Nature*, *375*, 47–50, doi:10.1038/375047a0.

Wilcock, W. S. D. (1998), Cellular convection models of mid-ocean ridge hydrothermal circulation and the temperatures of black smoker fluids, *J. Geophys. Res.*, *103*, 2585–2596, doi:10.1029/97JB03252.

Wilson, C., J.-L. Charlou, E. Ludford, G. Klinkhammer, C. Chin, H. Bougault, C. German, K. G. Speer, and M. Palmer (1996), Hydrothermal anomalies in the Lucky Strike segment on the Mid-Atlantic Ridge (37°17′N), *Earth Planet. Sci. Lett.*, *142*, 467–477, doi:10.1016/0012-821X(96)00100-8.